Journal of Geophysical Research: Oceans

RESEARCH ARTICLE
10.1029/2018JC014099

Key Points:
- The ocean mixed layer at 6 degrees south, 8 degrees east transitions from warm-fresh (December–April) to cold-salty (May–September)
- Solar heating and evaporative cooling are major determinants of the seasonal cycle in sea surface temperature at 6 degrees south, 8 degrees east
- Wind-driven upwelling and vertical mixing contribute to boreal summer SST cooling associated with equatorial cold tongue development

Correspondence to:
H. A. Scannell,
scanh@uw.edu

Citation:
Scannell, H. A., & McPhaden, M. J. (2018). Seasonal mixed layer temperature balance in the southeastern tropical Atlantic. *Journal of Geophysical Research: Oceans, 123*. https://doi.org/10.1029/2018JC014099

Received 19 APR 2018
Accepted 10 JUL 2018
Accepted article online 17 JUL 2018

Seasonal Mixed Layer Temperature Balance in the Southeastern Tropical Atlantic

Hillary A. Scannell[1,2] **and Michael J. McPhaden**[2]

[1]School of Oceanography, University of Washington, Seattle, WA, USA, [2]NOAA/Pacific Marine Environmental Laboratory, Seattle, WA, USA

Abstract Most climate models simulate sea surface temperatures (SSTs) that are consistently 1–4 °C warmer than observed in eastern tropical Atlantic. These biases undermine seasonal prediction efforts and the credibility of climate change projections in this region. To understand what drives the seasonal cycle in upper ocean temperature near the eastern boundary of the tropical Atlantic, we use a 5-year moored buoy data set from the Prediction and Research Moored Array in the Atlantic at 6°S, 8°E. The buoy is located along the southeastern edge of the Atlantic cold tongue where the seasonal cycle in SST, which is maximum in March and minimum in August, is influenced by the meridional movement of the Intertropical Convergence Zone (ITCZ) and formation of low-level marine stratocumulus clouds. Associated with these seasonal changes in atmospheric conditions, surface heat fluxes on seasonal timescales are most strongly controlled by shortwave radiation and latent heat flux. The seasonal mixed layer shoals, warms, and freshens in the boreal spring coincident with a southward migration of the ITCZ. The shallow mixed layer amplifies heating from solar radiation on mixed layer temperature at this time. Conversely, during the boreal summer, upwelling leads to entrainment of cold and salty water into the surface layer. From this analysis, we discuss the relative importance of the different components of the seasonal mixed layer heat balance at 6°S, 8°E and how they can be used to better understand the sources of climate model SST biases.

1. Introduction

The tropical Atlantic Ocean and atmosphere are strongly coupled through the transfer of heat, momentum, and moisture across the air-sea interface, with variability in these exchanges dominated by the seasonal cycle. In the eastern basin, the African continent plays an important role in shaping the structure of surface currents and consequently the distribution of sea surface temperature (SST). Along the eastern boundary, the warm Angola Current flows southward along the African coast to 15–17°S where it is met and deflected offshore by a cool equator-flowing Benguela Current. The strength and direction of these currents are modulated on seasonal and interannual timescales by local near-surface wind stress (Bachèlery et al., 2016; Richter et al., 2010) and remote forcing by equatorial and coastally trapped Kelvin waves (Bachèlery et al., 2016; Florenchie et al., 2003; Lübbecke et al., 2010; Rouault et al., 2007).

Wind patterns in the eastern tropical Atlantic associated with the Intertropical Convergence Zone (ITCZ) migrate latitudinally in response to the seasonal heating and cooling of the Northern and Southern Hemispheres. The meridional movement of the ITCZ and distribution of SST and sea surface salinity (SSS) are closely coupled and dominated by the seasonal cycle (Yu et al., 2006). The ITCZ can be traced by a band of heavy precipitation, increased high level clouds, and weakened wind speeds (Figure 1). During March, SSTs greater than 27 °C and heavy precipitation are zonally uniform and colocated between the equator and 5°S in the southeast Atlantic (Xie & Carton, 2004). Increased precipitation and river runoff decreases SSS in the Gulf of Guinea and along the eastern boundary during this time of year (Figure 1).

During the boreal summer, the ITCZ reaches its northernmost extent centered near 8°N associated with the onset of the West African Monsoon and formation of the equatorial cold tongue (Xie & Carton, 2004; Yu et al., 2006). Monsoon winds intensify in the Gulf of Guinea from an increase in convection and precipitation over the North African continent. Simultaneous strengthening of the South Atlantic anticyclone enhances upwelling of cold, saline water along the African coast and along the equator (Figure 1). Low-level marine stratocumulus clouds expand over the upwelled cold deep-water in the southeast Atlantic. These clouds reflect solar radiation and reinforce the cooling of SST. (Figure 1).

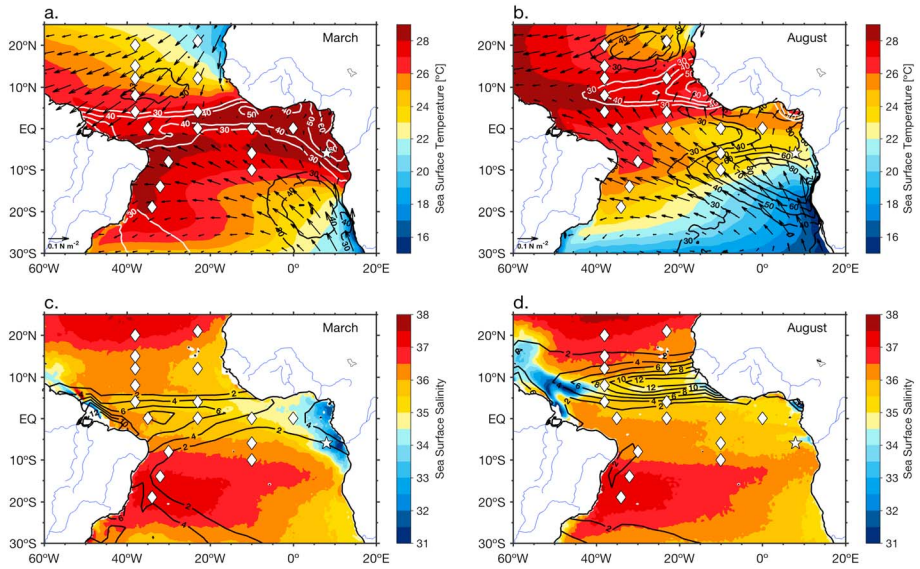

Figure 1. Climatological March and August snapshots of the tropical Atlantic. Mean (a) March and (b) August sea surface temperature (SST) and wind stress vectors with contoured percent cover of high level clouds (white lines) and low level clouds (black lines). Mean (c) March and (d) August sea surface salinity with contoured monthly averaged precipitation (mm/day). Locations of the Prediction and Research Moored Array in the Atlantic buoys are marked by diamonds and a star for the southeast extension (6°S, 8°E). Major rivers are shown over continents. Monthly wind stress data are from TropFlux between 1979 and 2017. Percentages of low (>680 hPa) and high (<440 hPa) level clouds (a and b) are retrieved from MODIS-Terra from 2002 to 2015 and represents the total fraction of a 1° latitude by1° longitude grid cell covered by clouds. Monthly precipitation (c and d) come from the Climate Prediction Center Merged Analysis of Precipitation from 1979 to 2017. SST is averaged from the daily optimum interpolation SST data set from 1981 to 2018 and sea surface salinity comes from the Soil Moisture Ocean Salinity mission available from 2010 to 2016.

Of particular significance to the southeast tropical Atlantic is the systematic errors in sea surface temperature in global climate models. Most models in phase 5 of the Coupled Model Intercomparison Project, for example, simulate sea surface temperatures that are too warm with respect to observations, especially along the coasts of Namibia and Angola. Biases in the southeastern tropical Atlantic range typically from 1 to 4 °C with the most severe warm biases up to 6–8 °C (Zuidema et al., 2016). This persistent and widespread problem is characteristic of earlier generations of Coupled Model Intercomparison Project models as well. The largest contribution to the warm biases is primarily the excessive solar insolation caused by the underestimation of low level marine stratocumulus clouds and from insufficient turbulent vertical mixing of cold water across the base of the mixed layer (Exarchou et al., 2017; Richter, 2015). It is suggested that SST biases in coupled climate models can feedback on cloud biases and influence the location of deep convection through large-scale circulation. As a consequence, systematic errors in deep convection also have the potential to shift the distribution of precipitation that influences horizontal gradients in SSS (Zuidema et al., 2016). These biases limit our ability to accurately simulate regional and global climate variability and change (Qu et al., 2014; Sherwood et al., 2014) and present a challenge in modeling and predicting droughts, floods, severe tropical storms, and hurricanes, which impact millions of people in the region. Process-based observational analyses are therefore needed to further understand what drives the seasonality of SSTs in regions with severe model bias.

Previous studies of the mixed layer temperature balance in the tropical Atlantic have benefited from data collected as part of the Prediction and Research Moored Array in the Tropical Atlantic (PIRATA). This network is comprised of 18 moored ocean buoys that continually measure oceanic and atmospheric conditions in the tropical Atlantic (Bourles et al., 2008; Figure 1). The moorings collect and transmit to shore in real-time high temporal resolution data to support the study of ocean-atmosphere interactions and ocean dynamics in the tropical Atlantic. Foltz et al. (2003) used these data to diagnose the mixed layer heat budget at eight PIRATA moorings in the northwest (8°N–5°N along 38°W), equatorial (between 10°W and 35°W) and southeastern (6°S–10°S along 10°W) areas of the basins. They found that off the equator the seasonal cycle of

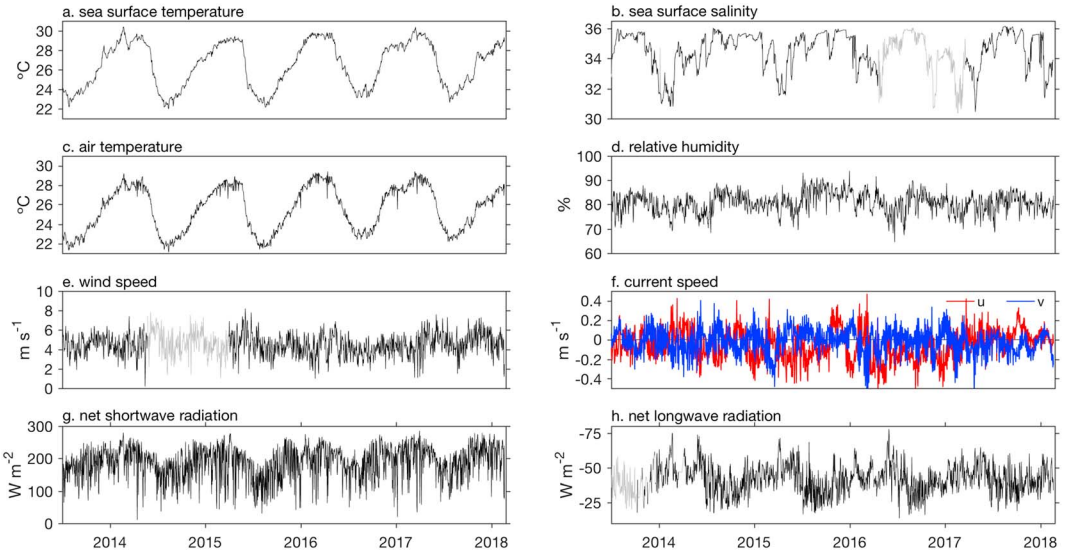

Figure 2. Daily ocean surface and meteorological measurements from the Prediction and Research Moored Array in the Atlantic-Southeast Extension mooring at 6°S, 8°E. Gaps in the data record for (e) wind speed and (h) net longwave radiation are extrapolated using a least squares regression with data from the TropFlux product. Missing data in (b) sea surface salinity are extrapolated from least squares regression of salinity at 1 and 5 m. Net longwave radiation assumes a broadband emissivity of 0.97 at the sea surface and net shortwave radiation assumes a surface albedo of 0.055. The sign convention is positive for surface heat flux into the ocean and vice versa.

mixed layer temperature is primarily balanced by latent heat loss and shortwave radiation, whereas along the equator the role of horizontal advection and entrainment becomes increasingly important. A model study by Yamagata and Iizuka (1995) at the off-equatorial location of 10°S, 9°E also found that surface fluxes drive the seasonal cycle, with cooling March through August and warming September through February.

The mooring at 6°S, 8°E did not exist at the time that Foltz et al. performed their analysis. This mooring is in an oceanic region that has been historically undersampled and where model SST biases are relatively large compared to other PIRATA sites (Zuidema et al., 2016). This site is also of interest because it sits on the southeastern edge of the Atlantic cold tongue where upwelling and turbulent entrainment may contribute to the seasonal evolution of mixed layer temperature (e.g., Foltz et al., 2003). We describe in detail the various processes that give rise to the seasonal evolution of SST at this site and discuss the implications of our results for climate model SST biases in the southeastern tropical Atlantic.

2. Data and Methods

2.1. PIRATA-Southeast Extension 6°S, 8°E

Since the initial implementation of PIRATA in 1997 (Servain et al., 1998), the array has undergone a series of extensions and enhancements. One of these expansions includes the PIRATA-Southeast Extension (PIRATA-SEE) at 6°S, 8°E that was initiated in 2005 (Rouault et al., 2009). A pilot phase began in June 2006 through June 2007, and the mooring has been continually operational since June 2013. We use the daily data record from PIRATA-SEE since June 2013, which extends almost 5 years to present (Figure 2).

The PIRATA-SEE site was occupied with an Autonomous Temperature Line Acquisition System mooring from 2013 to 2017 and later with a functionally equivalent T-Flex system beginning in March 2017. Subsurface temperature is available at 14 depth intervals from 1 to 500 m and subsurface salinity at 9 depth intervals from 1 to 120 m. Temperature is sampled at 1, 3, 5, 10, 20, 40, 60, 80, 110, 120, 140, 180, 300, and 500 m, and subsurface salinity is sampled at 1, 3, 5, 10, 20, 40, 60, 80, and 120 m. Subsurface temperature and salinity at 3 m was not available until late March 2017 with the implementation of the T-Flex mooring sensor upgrade. We refer to the 1-m values of temperature and salinity as SST and SSS, respectively. Temperature and salinity are measured hourly and are available from the National Oceanic and Atmospheric Administration/Pacific Marine Environmental Laboratory Global Tropical Moored Buoy Array

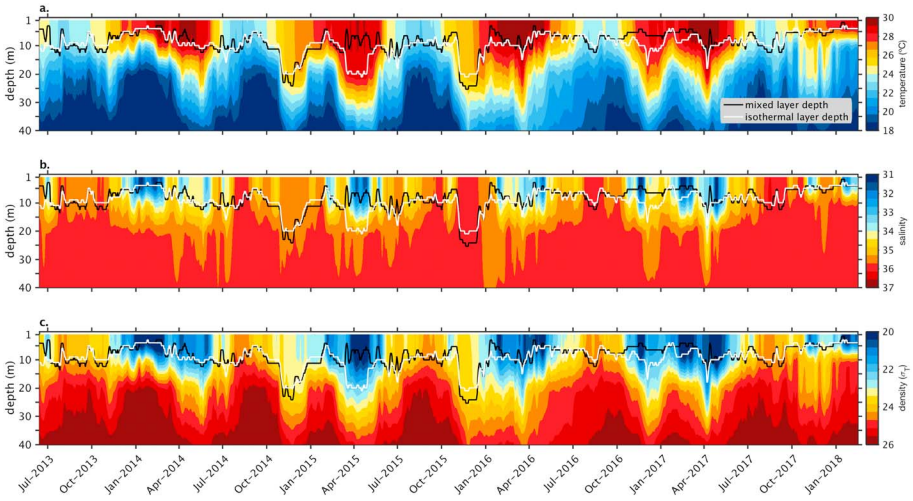

Figure 3. Upper ocean hydrographic structure at the Prediction and Research Moored Array in the Atlantic-Southeast Extension buoy from June 2013 to February 2018. Daily profiles of (a) temperature, (b) salinity, and (c) density (σ_T) in the upper 40 m are vertical interpolated to a 1-m resolution and smoothed temporally with a 7-day triangle filter to eliminate high-frequency variability. Mixed layer depth (black line) and isothermal layer depth (white line) are calculated for each interpolated profile using a 0.3 °C temperature decrease from a 1-m reference level.

Project website (https://www.pmel.noaa.gov/gtmba/). For the purposes of this study, we use daily averages computed from higher-resolution hourly data.

Temporal gaps in daily subsurface salinity at 1 and 5 m toward the end of the record are filled using orthogonal linear least squares regression relationships between 10 and 1 m and 10 and 5 m, respectively. Salinity covaries significantly across depths within the upper 10 m, so that a linear regression model using 10 m salinity predicts 92.8% of the variance in 5-m salinity, and 92.6% of the variance in 1-m salinity. The root-mean-square error is 0.74 for 5-m salinity estimates and 0.77 for 1-m salinity estimates. After filling gaps in the time series, subsurface temperature and salinity profiles are linearly interpolated in the vertical to 1-m resolution. Subsurface density (σ_T) is then computed from temperature and salinity. Vertical profiles of temperature, salinity, and density show a strong seasonal cycle in a very shallow mixed layer (Figure 3).

Instrumental accuracy is ±0.02 °C and ± 0.02 for temperature salinity respectively (A'Hearn et al., 2002; Freitag et al., 1999, 1995, 2016). A single-point acoustic-Doppler current meter at 10-m depth measures both zonal and meridional current velocities at an hourly sampling interval with ±5 cm/s accuracy (Plimpton et al., 1995, 2004). Near-surface air temperature and relatively humidity are sampled at 10 min intervals 3 m above the sea surface and have accuracy within ±0.2 °C and ± 2.7% respectively (Lake et al., 2003). Rainfall is sampled every 10 min from a gauge 3 m above the sea surface with ± 0.4 mm/hr accuracy (Serra et al., 2001). Shortwave and longwave radiation is measured every 2 min from sensors 3.5 m above the sea surface with instrument accuracy ±2% and ± 1%, respectively (Cronin & McPhaden, 1997). Net shortwave radiation assumes a surface albedo of 5.5% and net longwave radiation assumes a sea surface emissivity of 0.97. An anemometer at 4 m above the sea surface records wind speed every 10 min with accuracy ±0.3 m/s (Freitag et al., 2001).

We fill gaps in wind speed and net longwave radiation using an orthogonal least squares linear regression based on the relationships between the PIRATA-SEE data and the TropFlux reanalysis of air-sea heat and momentum flux (Kumar et al., 2013; Figure 2). TropFlux, available from 1979 onward, is derived from the European Reanalysis-Interim and the International Satellite Cloud Climatology Project and has been bias- and amplitude-corrected based on the Global Tropical Moored Buoy Array (Kumar et al., 2013). TropFlux longwave radiation explains 81.3% of variance in net longwave radiation measured at the PIRATA-SEE buoy. TropFlux wind speed data are located at 10 m above the sea surface. To compare with PIRATA, we adjust the 4-m PIRATA wind speed data to 10 m using the neutral wind equation following Smith (1988), which assumes that wind speed increases logarithmically with height to a first approximation. TropFlux wind speed explains 91.7% of variance of the adjusted wind speed measured at the PIRATA-SSE buoy.

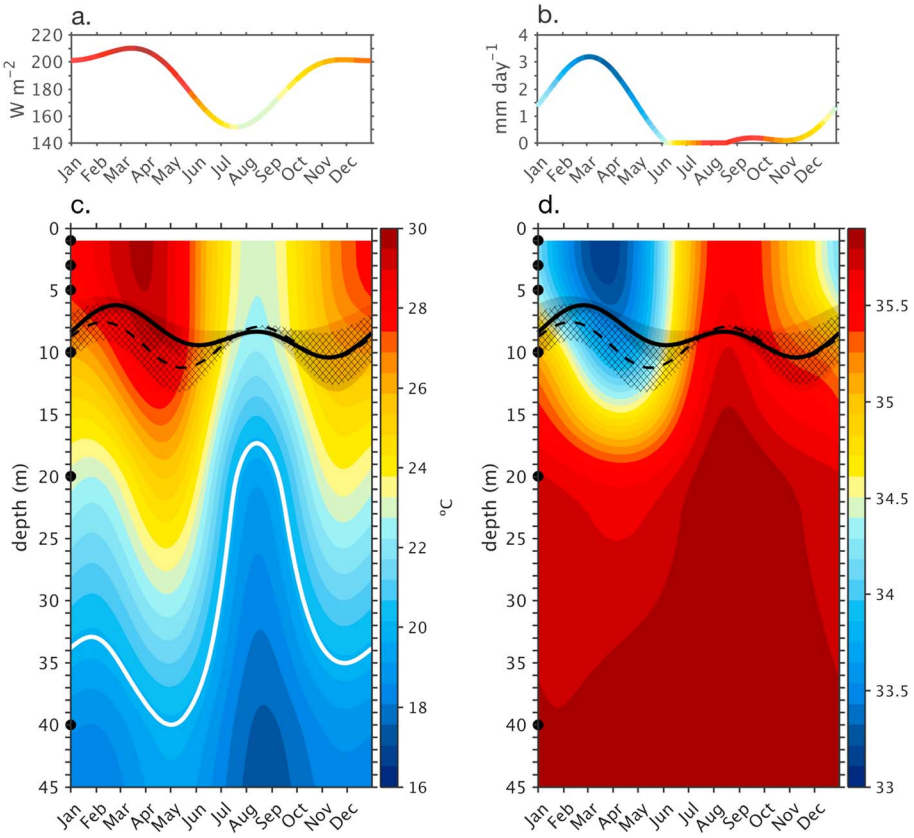

Figure 4. Seasonal cycles of mixed layer temperature and salinity 6°S, 8°E. Mixed layer temperature and salinity are influenced by (a) net downwelling shortwave radiation and (b) precipitation measured at the Prediction and Research Moored Array in the Atlantic buoy with a color encoding that corresponds to the average mixed layer temperature and salinity, respectively. Upper 40-m (c) temperature with 20 °C isotherm depth (white line), mixed layer depth (solid black line), and isothermal layer (dashed black line), and (d) salinity show water column stratification. Mixed layer temperature and salinity are computed as the integration of values from the sea surface to the base of the mixed layer. The mixed layer depth is defined as a 0.08 kg/m^3 density (σ_T) increase from a 1-m reference level, and its standard error (gray shading) is based on interannual anomalies the 2013–2018 mean seasonal cycle. The isothermal layer depth (dashed line) is defined as the depth at which temperature decreases 0.3 °C from a 1-m reference level and is shown with its monthly standard error (cross hatches). Dark circles in (c) and (d) represent the depths of direct PIRATA measurements used to linearly interpolate data to a 1 m vertical resolution.

To describe the seasonal cycle in the southeast tropical Atlantic, we analyze the mixed layer heat budget using data available from PIRATA-SEE at 6°S, 8°E. To eliminate high-frequency variability, we fit daily data with mean, annual, and semiannual harmonics using least squares regression. Daily profiles of temperature and salinity are fit using this procedure to show seasonal variations in the upper 45 m (Figures 4c and 4d). We expect that the largest source of uncertainty given the short observational record will be from sampling errors estimated from deviations about the harmonic fits to the data and that instrumental and computational errors are relatively small compared to these errors. Errors in this analysis are therefore expressed as 1 standard error based on year-to-year deviations from the mean seasonal cycle.

2.2. Heat Balance

The processes responsible for determining mixed layer temperature are represented by the following balance of terms (Moisan & Niiler, 1998; Stevenson & Niiler, 1983):

$$\rho c_p h \frac{\partial T}{\partial t} = -\rho c_p h(\mathbf{v}\cdot\nabla T\ ) + q_o + \varepsilon. \tag{1}$$

From left to right, the terms in (1) represent the time rate of change of mixed layer heat storage, which is balanced by mean horizontal heat advection, net surface heat flux absorbed in the mixed layer, and a

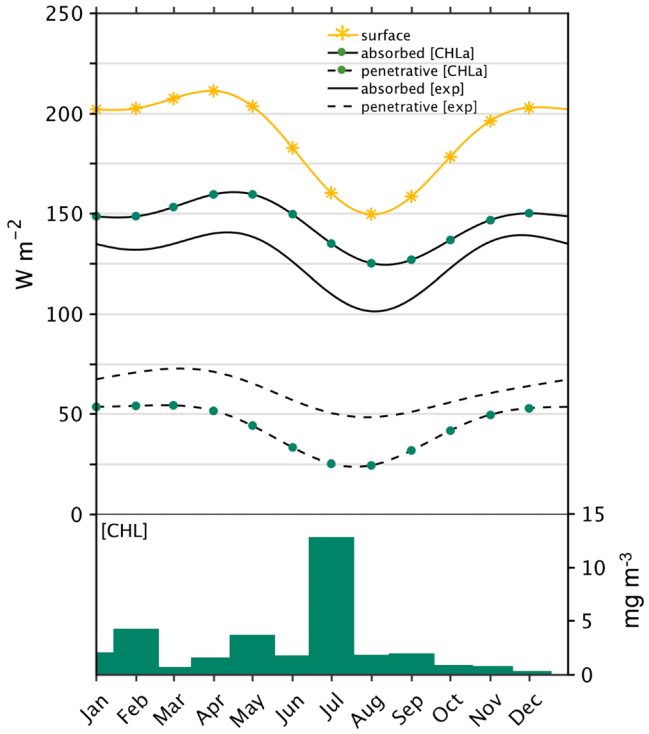

Figure 5. Seasonal cycles of downwelling surface radiation, estimated absorbed radiation within the mixed layer and penetrative shortwave radiation at the base of the mixed layer at 6°S, 8°E. Two methods are compared: (1) using a 25 m *e*-folding decay of net surface shortwave radiation to estimate the amount absorbed (solid black line) and penetrative (dashed black line) and (2) using an empirical approximation based on the concentration of chlorophyll-*a* at the sea surface to compute the absorbed (solid green dot line) and penetrative (green dash-dotted line) radiation. The monthly climatology of chlorophyll-*a* concentration is estimated from the MODIS-Aqua mission. All data are monthly averaged and fit with mean, annual, and semiannual harmonics.

residual term. Parameters in equation (1) include the mixed layer density (ρ), specific heat of seawater (c_p), mixed layer depth (h), and the time rate of change of the vertically averaged mixed layer temperature (T). Horizontal advection is a function of the vertically averaged mixed layer velocity ($\mathbf{v}$) and the horizontal gradient of mixed layer temperature.

Net surface heat flux (q_o) is the sum of net downwelling shortwave radiation (SWR) minus the shortwave radiation that penetrates through the base of the mixed layer (SWR_{pen}), net longwave radiation (LWR), latent (LHF), and sensible heat fluxes (SHF), such that

$$q_o = \left(\mathrm{SWR} - \mathrm{SWR_{pen}}\right) + \mathrm{LWR} + \mathrm{LHF} + \mathrm{SHF}. \quad (2)$$

The penetration of shortwave radiation through the mixed layer is controlled by the optical properties of the mixed layer and its depth. As in Foltz et al. (2003), we evaluate two models to estimate shortwave penetration. The first is a chlorophyll-dependent empirical model for penetrative shortwave radiation that takes into account biological productivity using chlorophyll-*a* concentration, $Q_{pen} = 0.47Q_{surf}\, e^{-\left(0.027+0.518CHL^{0.428}\right)h}$ (Morel, 1988). The amount of penetrative shortwave radiation relies on the surface shortwave radiation (Q_{surf}), satellite-derived chlorophyll-*a* concentration (CHL) from National Aeronautics and Space Administration Moderate Resolution Imaging Spectroradiometer-Aqua (MODIS-Aqua) and the depth of the mixed layer (h). We compute the monthly climatology of the satellite derived chlorophyll-*a* concentration (mg/m^3) averaged across 5–7°S and 7–9°E to find the monthly climatology of penetrative shortwave radiation. We compare the empirical model with one that assumes a 25-m *e*-folding decay of shortwave radiation, $Q_{pen} = 0.45Q_{surf}\, e^{-\gamma h}$, where γ is the decay rate constant, 0.04 m^{-1} (Wang & McPhaden, 1999). Gamma is set to larger values in biologically productive regions or near high river runoff. Both models have similar seasonal cycles; however, there is a 12–26 W/m^2 bias seasonally between the two radiation models where the chlorophyll-based model always estimates more absorbed shortwave radiation than the exponential decay model (Figure 5). The influence of high biological productivity in a region with shallow mixed layers exerts a large effect on the total absorbed shortwave radiation. We therefore use the empirical chlorophyll-*a* model to derive penetrative shortwave radiation in this analysis.

Absorbed shortwave radiation is determined from equation (2) as the difference between downwelling shortwave radiation at the surface and that which penetrates through the base of the mixed layer. To understand the seasonal effects of clouds on the mixed layer heat budget, we compare the absorbed shortwave radiation with the noontime maximum in solar radiation when no clouds are present (Figure 6). The clear-sky global horizontal irradiance is calculated using the Adnot-Bourges-Campana-Gicquel model

$$\mathrm{GHI} = 951.39\cos(\theta_z)^{1.15}, \quad (3)$$

which is a univariate function of the solar zenith angle (θ_z) at 6°S (Badescu, 1997).

Turbulent heat fluxes are estimated using the Coupled Ocean-Atmosphere Response Experiment version 3.5 bulk flux algorithms (Fairall et al., 2003). Version 3.5 has improved parameterizations of the surface roughness and drag coefficients used to estimate surface stress from bulk formulas (Edson et al., 2013). Latent heat flux is dependent on surface humidity, wind speed, air temperature, and SST, $Q_{lhf} = \rho_a L_E C_L\{W\Delta q\}$, where ρ_a is the air density, L_E is the latent heat of vaporization, C_L is the transfer coefficient, W is wind speed, and Δq is the difference between surface saturation at the sea surface and air humidity. Sensible heat flux relies on wind speed and the temperature difference between the sea surface and atmosphere $Q_{shf} = \rho_a C_p C_s\{W\Delta T\}$, where C_p is the specific heat capacity of air, C_s is the transfer coefficient, and ΔT is the air-sea temperature difference.

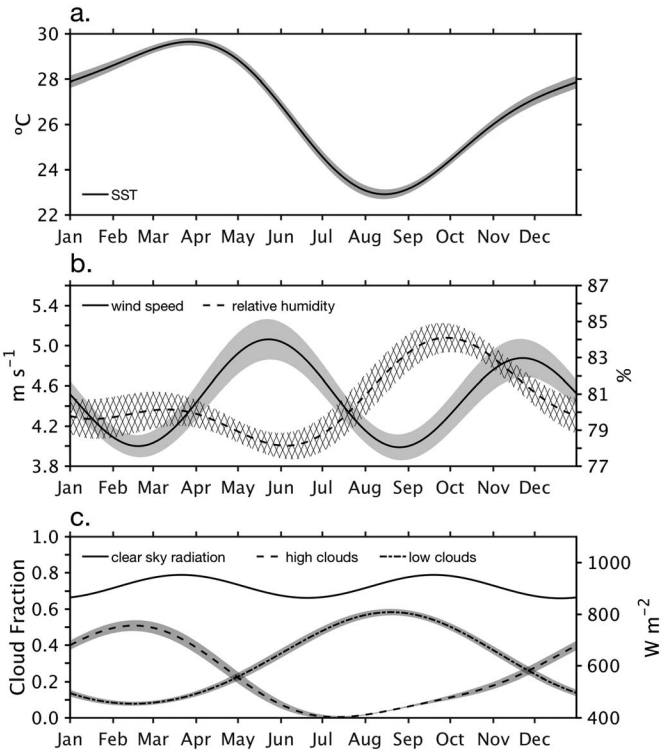

Figure 6. Mean seasonal cycle of (a) sea surface temperature, (b) 10-m wind speed and relative humidity, and (c) high and low cloud fraction, and clear-sky radiation at 6°S, 8°E. Shading represents the standard error of monthly averaged terms fit to the seasonal cycle.

We define the depth of the ocean mixed layer based on a density difference from a near-surface reference level. This definition takes into consideration the influence of salinity on upper ocean stratification. When a shallow halocline persists above a deeper thermocline, barrier layers can form that prevent mixing between the surface mixed layer and thermocline waters (Foltz & McPhaden, 2009). The barrier layer is a region between the thermocline and surface mixed layer that decouples the two regions by limiting vertical turbulent transfers between them. When barrier layers exist, the mixed layer defined in terms of temperature alone results in an overestimation of the true mixed layer depth. Thus, we use the mixed layer depth definition according to Sprintall and Tomczak (1992), $\sigma_t(h) = \sigma_t(h_r) + \Delta T \frac{\partial \sigma_t(h_r)}{\partial T}$, where the mixed layer depth (h) is defined where the density (σ_t) at 1-m reference level (h_r) increases to a density equivalent of a 0.3 °C temperature change (ΔT) (Figure 3). Our choices for h_r and ΔT were chosen based on sensitivity analyses with different values. The mixed layer is most sensitive to the reference level, and 1 m is chosen because the mixed layer can be as shallow as 5 m and it is a noninterpolated depth value measured directly at the mooring. A temperature change of 0.3 °C is equivalent to a 0.08 kg/m^3 density increase and is consistent with other heat budget studies (e.g., Foltz et al., 2013).

The vertical resolution of PIRATA temperature and salinity measurements used to compute mixed layer depth varies from 2 to 10 m in the upper 20 m of the water column. Seasonal fluctuations in mixed layer depth are found to be small and on the order of 5 m. To understand the sensitivity of the mixed layer depth calculation to vertical resolution, we use 186 higher vertical resolution Argo profiles within ±2° latitude and longitude of the PIRATA mooring (see Appendix A). We find that coarser vertical resolution of PIRATA data yields mixed layers that are on average about 20% too shallow. We therefore correct the PIRATA-derived mixed layer depths using a regression equation based on comparison with the Argo data and use this adjusted mixed layer depth throughout the remainder of the paper (Figure A1).

We use the zonal and meridional velocity measurements from the at 10-m current meter to compute horizontal advection in the mixed layer. We assume that the velocity at 10 m is representative of the mixed layer, which varies between 5 and 15 m, recognizing that there are times when 10 m is just below the mixed layer. We approximate the horizontal gradients in mixed layer temperature using the satellite derived daily optimum interpolation SST data set that has a 0.25° latitude by 0.25° longitude resolution (Reynolds et al., 2007). We take horizontal gradients of optimum interpolation SST using a centered difference over ± 0.375° latitude and longitude domain centered at 6°S, 8°E. The horizontal scale for this calculation was chosen based on the time that a water parcel would take to travel across this distance at the observed velocity. Horizontal current velocities at 6°S, 8°E have a standard deviation of 13.4 km/day zonally and 11.2 km/day merdionally so that it would take a water parcel approximately 1 week to advect through this region.

The residual heat flux (ε) represents the combination of accumulated instrumental, sampling, and computational errors in the explicitly resolved terms plus any neglected physical processes, the most important of which are vertical turbulent transfers of heat involving diffusion and/or entrainment across the base of the mixed layer (Foltz et al., 2003). Turbulent processes cannot be directly measured from the buoy data. However, the upper bounds can be estimated by assuming that ε is all due to turbulence rather than any noise contamination (McPhaden, 1982; Wang & McPhaden, 1999). For the sake of argument, we will further assume the turbulent processes involve entrainment of thermocline water across the base of the mixed layer although it is also possible that diffusive processes may be operative as well. With these assumptions, the upper bound on turbulent entrainment velocity (W_e) is given by

$$W_e = -\frac{\varepsilon}{\rho_0 C_p \delta T} \quad (4)$$

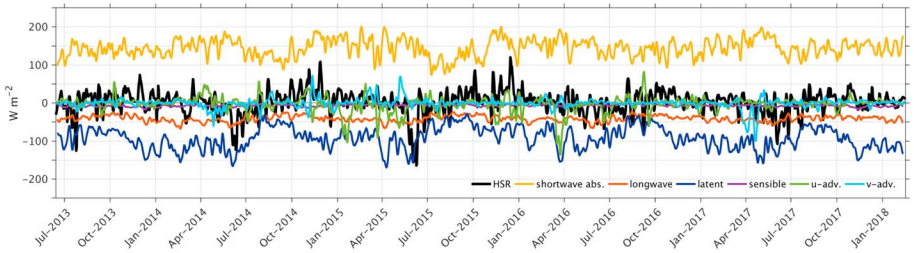

Figure 7. Components of the mixed layer heat balance at 6°S, 8°E from Prediction and Research Moored Array in the Atlantic-Southeast Extension. Daily data are smoothed temporally with a 7-day triangle filter to eliminate high frequency variability. The components that balance the total heat storage rate (HSR) are absorbed shortwave and net longwave radiation, latent and sensible turbulent heat flux, and zonal (u-adv) and meridional (v-adv) heat advection. Positive terms are interpreted as heating the ocean mixed layer and negative terms as cooling.

where (δT) is the temperature difference between the mixed layer and a depth 20 m below the mixed layer (Chang, 1993).

Terms in equations (1)–(4) are computed using daily data smoothed with a 7-day triangle filter to eliminate high frequency variability (Figure 7). Daily data are then fit to mean, annual, and semiannual harmonics to define the seasonal cycle. Sampling errors are expressed as 1 standard error from this fitting procedure.

3. Results

In the following section, we describe the seasonal variability of various processes that affect the surface layer heat balance followed by a detailed examination of the terms in the balance itself at the 6°S, 8°E PIRATA buoy. We begin with a description of the vertical structure of upper ocean temperature and salinity, which is dominated by the annual and semiannual cycles (Figures 4c and 4d). The base of the mixed layer exhibits a semiannual cycle with shoaling during the boreal winter and summer over a vertical depth range of less than 5 m (solid black lines in Figures 4c and 4d). Early in the year, the mixed layer warms and freshens in response to high austral summer insolation and precipitation (Figures 4a and 4b) as the ITCZ moves toward its southernmost latitude (Figure 1).

Surface salinity influences the processes controlling mixed layer temperature through changes in mixed layer density and depth. Near-surface freshening during the boreal spring forms a shallow halocline above the seasonal thermocline that can produce barrier layers where the mixed layer based on density is shallower than the isothermal layer. Barrier layer thickness is defined as the difference between the mixed layer and isothermal layer as, for example, illustrated in Figures 3 and 4c and 4d. Barrier layers can limit the mixing of cold thermocline waters into the near-surface layer; however, we find that when averaged to seasonal timescales, the thickness of the barrier layer in boreal spring is thin (Figures 4c and 4d); moreover, the difference between the mixed layer and isothermal layer is not statistically significant. Thus, on seasonal timesscales, barrier layers most likely do not have a large effect, though barrier layers may play a more significant role on subseasonal timescales (e.g., Figure 3).

During the boreal summer, SST rapidly decreases coincident with a reduction in shortwave radiation due to a seasonal maximum in solar zenith angle and the expansion of the stratocumulus cloud deck (Figures 4a and 6c). Low-level stratocumulus clouds form over cold surface water and reflect sunlight back to space, significantly reducing solar radiation at the surface. Marine stratocumulus clouds that form over cold water thus further cool SSTs in the boreal summer. Cold SST in turn increases the stability of the marine boundary layer and confine low-level and highly reflective marine stratocumulus clouds to the lower troposphere near the descending branch of the Hadley Cell (Wood, 2012).

The stratus deck in the southeastern tropical Atlantic is prominent only in the boreal summer, so that insolation exhibits a primarily 1 cycle per year variation with a minimum in boreal summer (Figure 4a) even though clear-sky radiation shows a 2 cycle per year variation (Figure 6c; see also Li & Philander, 1997). However, the amount of solar radiation absorbed by the ocean mixed layer is also dependent on the optical properties of the water. During summer, surface chlorophyll-*a* concentrations are a maximum in July when upwelling

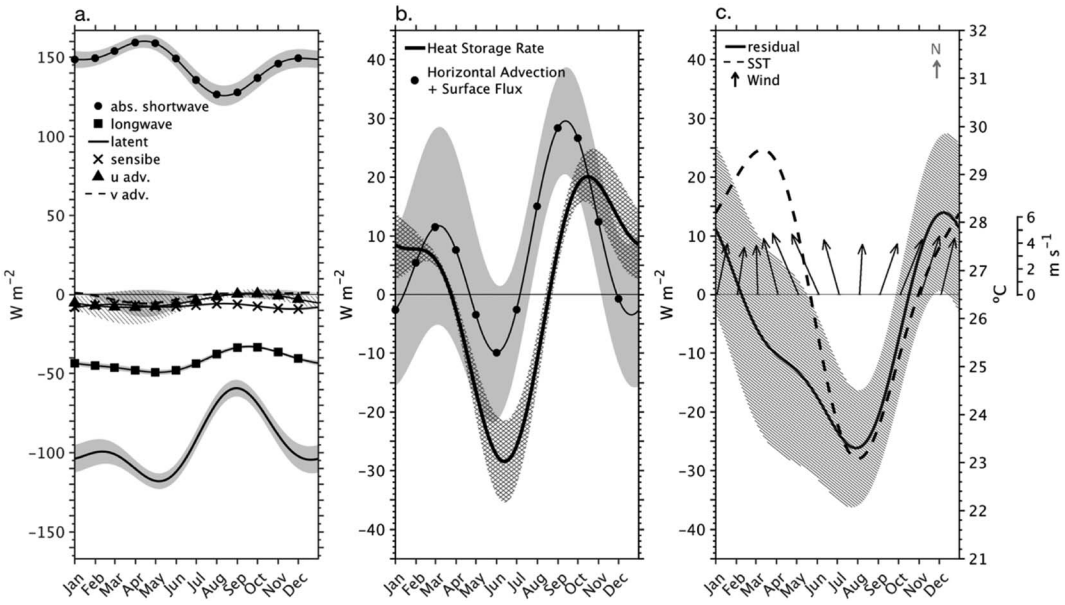

Figure 8. Seasonal mixed layer heat balance at 6°S, 8°E at the Prediction and Research Moored Array in the Atlantic-Southeast Extension. (a) The mean seasonal cycle of the different components in the surface mixed layer heat balance, (b) total heat storage rate and sum of horizontal advection (u-adv and v-adv) and surface flux (absorbed shortwave, longwave, latent, and sensible), and (c) residuals computed as the total heat storage rate minus the sum of horizontal advection and surface flux terms, sea surface temperature, and wind speed and direction. Shading representing uncertainty computed as one standard error of monthly values fit to the seasonal cycle.

replenishes cold, nutrient-rich water to the sea surface and boosts biological productivity (Figure 5). An abundance of phytoplankton that contain chlorophyll absorb and scatter shortwave radiation within the mixed layer and decrease the amount of penetrative radiation escaping the base of the mixed layer (Figure 5). Thus, phytoplankton change the optics of the upper ocean during the boreal summer thereby increasing the attenuation of solar radiation with depth.

Latent heat flux is dependent on wind speed as well as the difference between the saturation specific humidity of the sea surface and the specific humidity of the air just above. This air-sea humidity difference is large when the relative humidity of the air is low and vice versa. In May and June, a weak seasonal minimum of relative humidity (78%) and maximum in wind speed (5 m/s) increase evaporation at the sea surface and enhance cooling in the mixed layer (Figure 6b). Conversely in September, a maximum in relative humidity above the sea surface (84%) coincides with a minimum in wind speed (4.1 m/s) that reduces the efficiency of evaporative cooling at the sea surface. These predominantly semiannual variations of wind speed and annual variations in relative humidity lead to both annual and semiannual variations in latent heat loss, with a pronounced minimum in heat loss during August–October (Figure 8a).

Sea surface salinity reaches a seasonal maximum during the late boreal summer coincident with a minimum in SST (Figure 4c). The seasonal peak in surface salinity is enhanced by the northward displacement of the ITCZ that reduces freshwater supply from local precipitation and river runoff at this time (Figure 1). The mixed layer and isothermal layer shoal in boreal summer are coincident with a rapid upwelling of the thermocline (Figure 4c). Upwelling advects cold, saline thermocline water toward the surface where it can be efficiently entrained into the mixed layer. The depth of the thermocline can be estimated by the 20 °C isotherm, which has both annual and semiannual components that varies from a depth of 19–40 m (Figure 4c, white line). Local winds do not appear to drive this upwelling, since winds that are southerly all year (Figure 8) have their minimum speeds during this season (Figure 6b). Cold SSTs stabilize the atmospheric boundary layer in the boreal summer by minimizing the downward vertical atmospheric momentum flux, which results in weaker surface winds (Hayes et al., 1989; Wallace et al., 1989). As SSTs warm, atmospheric stratification erodes allowing more efficient mixing between the boundary layer and the free atmosphere, causing the southeasterly trades to intensify (Hayes et al., 1989). These wind field variations in relation to SST have been observed in

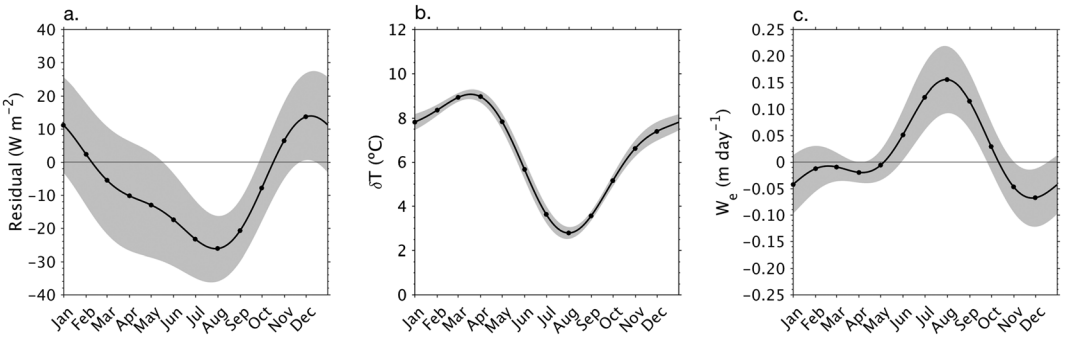

Figure 9. Seasonal cycle of the (a) mixed layer heat budget residuals (replotted from Figure 8c), (b) vertical temperature difference between the mixed layer and 20-m below the base of the mixed layer (δT), and (c) inferred turbulent entrainment velocity (W_e) across the base of the mixed layer. Light shading represents 1 standard error.

the cold tongue regions of the equatorial Pacific (Wallace et al., 1989) and Atlantic (De Coëtlogon et al., 2013) and are evident in the relation of wind speed (Figure 6a) to the seasonal cycle of SST (Figure 4c) at 6°S, 8°E.

Remote wind forcing rather than local wind forcing is most likely responsible for driving upwelling at this location. Yamagata and Iizuka (1995) have pointed out that semiannual relaxation of the trade winds west of 30°W will generate downwelling Kelvin waves that propagate eastward into the Gulf of Guinea deepening the thermocline there in March and November. In addition, easterly trade winds intensify in boreal summer in the central equatorial Atlantic as the ITCZ migrates northward forcing an eastward propagating upwelling Kelvin wave (Weisberg & Tang, 1990). The buoy at 6°S, 8°E is situated off the equator in a region of maximum amplitude for first meridional mode Rossby waves that would be generated from the boundary reflection of remote wind-driven equatorial Kelvin waves (Ding et al., 2009). The superposition of remotely forced and reflected long wave most likely explains the seasonal variations in thermocline depth at 6°S, 8°E.

We now turn to the specifics of how the rate of heat storage rate in the mixed layer is influenced by horizontal advection, surface radiative and turbulent heat fluxes, and vertical turbulent processes (Figure 8). Absorbed shortwave radiation and latent heat loss are the largest terms in the surface energy balance and have pronounced seasonal cycle (Figure 8a). The seasonal cycle of latent heat flux due to evaporation is out of phase with absorbed shortwave radiation and cools the mixed layer more strongly in the boreal spring than summer. Sensible heat flux cools the mixed layer throughout the year but is less than -10 W/m^2 with a negligible seasonal cycle. Net longwave radiation is nearly constant at -40 W/m^2 and also has a small seasonal cycle (Figure 8). Horizontal advection has a weak seasonal cycle that is not distinguishable from zero within the error bounds (Figure 8a).

The sum of the terms calculated here does not balance the rate of heat storage. There is missing a source of cooling in the boreal summer indicated by significant negative residuals in June through September ranging from -17.4 W/m^2 to -26.2 W/m^2 (solid back line in Figure 8c). We interpret these residuals as due to turbulent entrainment. Using vertical temperature changes at the base of the mixed layer, we determine how large turbulent entrainment velocity would need to be to account for the residual heat flux during these months. We find that largest residuals (July and August) are associated with relatively small vertical temperature gradients and significant W_e values (Figure 9). The maximum seasonal W_e occurs in August coincident with the largest negative residual in the mixed layer heat balance (Table 1). This demonstrates that vertical entrainment processes are likely to be important to the mixed layer heat balance during the boreal summer months and plausibly explain the missing source of mixed layer cooling during this time of year. These results are consistent with the mixed layer heat balance by Foltz et al. (2003) at 0°, 10°W who showed the residual heat flux in summer was as large as ~100 W/m^2 and that entrainment, calculated as the mass flux across the base of the mixed layer, was most important during the boreal summer. Similarly, in Wang and McPhaden (1999) the residual heat budget flux in the eastern equatorial Pacific at 0°, 110°W was as large as ~120 W/m^2 during the boreal summer, which is ~5–10 times larger than found here. Interpreted as entrainment, their estimate of W_e was likewise 10 times larger than ours. One explanation for these differences is that that upwelling and

Table 1
Monthly Significant Negative Nonzero Residuals in the Mixed Layer Temperature Balance at 6°S, 8°E, Temperature Difference Between the Mixed Layer and 20 m Below the Base of the Mixed Layer (δT), and the Turbulent Entrainment Velocity (W_e) Across the Mixed Layer

	June	July	August	September
Residual (W/m^2)	−17.43 ± 16.49	−23.27 ± 8.93	−26.16 ± 10.57	−20.73 ± 9.76
δT (°C)	5.66 ± 0.48	3.63 ± 0.21	2.78 ± 0.33	3.56 ± 0.25
W_e (m/day^1)	0.05 ± 0.05	0.12 ± 0.06	0.16 ± 0.06	0.12 ± 0.05

Note. Uncertainty is displayed as 1 standard error based on deviations from the mean seasonal cycle.

entrainment on the equator are more vigorous in the cold tongue region than at 6°S so that both heat budget residuals and estimates of W_e are smaller at the PIRATA-SEE site.

4. Summary

In this study we examined the seasonal mixed layer heat balance in the southeast tropical Atlantic using 5 years of observations collected from the PIRATA-SEE mooring at 6°S, 8°E, combined with satellite and reanalysis data. Our purpose was to determine the factors responsible for the seasonal evolution of mixed layer temperature. We found that the seasonal evolution of mixed layer temperature has two pronounced regimes: a warm-fresh regime (December–April) and a cold-salty regime (May–September).

The warm-fresh regime (December through April) is characterized by high surface shortwave radiation and precipitation that increase near-surface stratification, leading to a shallow mixed layer. Solar heating is very efficient in warming SST at this time since heat is trapped in a relatively thin mixed layer. Warming and freshening of the mixed layer is associated a southward migration of the ITCZ that increases local precipitation and river runoff from the Congo River. The mixed layer is warmed primarily through shortwave radiation, which reaches maximum values in boreal spring at this location. Conversely, horizontal advection from the poleward flowing Angola Current contributes little to the heat balance at this location.

The mixed layer transitions to cool and salty during the boreal summer (May through September) when the equatorial cold tongue develops. This cool and salty regime is driven by the intensification of the southeasterly Trades in response to the onset of the West African Monsoon and the displacement of the ITCZ further north (Mitchell & Wallace, 1992). The strengthened Trades enhance local evaporative cooling and upwelling along the African coast as well as along and south of the equator. The mixed layer shoals in August when cold and salty thermocline water is entrained into the mixed layer. Cool SSTs stabilize the shallow stratocumulus cloud deck along the eastern boundary, shielding the ocean surface from downwelling shortwave radiation, which is a minimum at this time of year. The mixed layer gradually warms and freshens following this period through processes controlled by the position of the Sun overhead and southern migration of the ITCZ.

The residuals of the explicitly calculated terms in the heat budget include various sources of error and neglected physical processes, the most important of which is related to vertical turbulent mixing. We attribute the residual cooling in the mixed layer during June through August primarily to vertical turbulent entrainment enabled by upwelling favorable conditions at this time (e.g., Camara et al., 2015; Da-Allada et al., 2013; Tzortzi et al., 2013). The residual heat flux in June through September and inferred entrainment velocities are about 5–10 times smaller than found right on the equator in the eastern Pacific and Atlantic, consistent with the notion that upwelling and entrainment during the boreal summer are more vigorous on the equator than at the poleward margins of the equatorial cold tongue.

Our results are consistent with previous studies that found that surface fluxes dominate the annual cycle of SST off the equator, while ocean dynamics play a more important role between 5°S and 10°N (Carton & Zhou, 1997; Foltz et al., 2003; Yu et al., 2006). Our results also suggest that precipitation is an important component toward understanding the heat balance in the eastern tropical Atlantic since the fresh water flux into the ocean leads to shallow mixed layers in the early part of the calendar year. This work motivates collection of temperature, salinity, and velocity observations with finer vertical resolution in upper ocean to more accurately document and understand the physical processes involved.

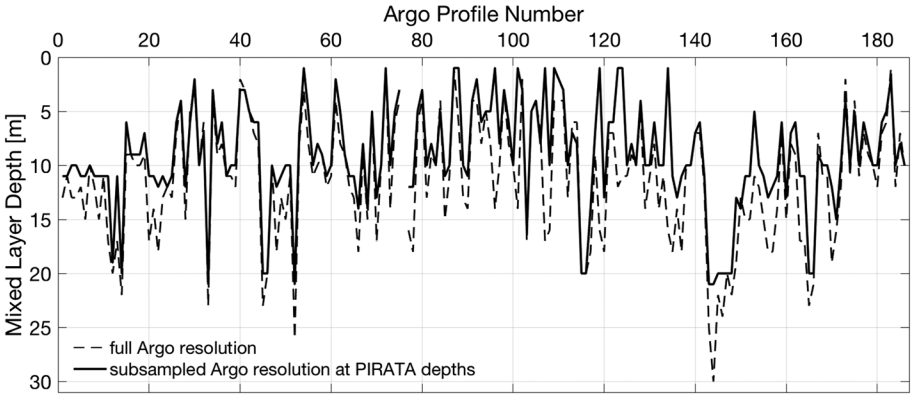

Figure A1. Comparison of Argo profile mixed layer depths and the adjusted mixed layer depth using the regression relationship between data at high and coarse vertical resolution.

These findings indicate that the distribution of SST is highly sensitive to surface fluxes in the southeastern tropical Atlantic where the most severe climate model biases occur. In particular, absorbed shortwave radiation is dependent on low-level cloud cover, which is often misrepresented in climate models. An underestimation of the stratocumulus cloud deck allows excessive absorption of shortwave radiation to reach the sea surface and contributes strongly to the SST warm biases in the eastern tropical Atlantic (Zuidema et al., 2016).

Previous evaluations of coupled climate models suggest that a variety of factors are involved in creating these SST biases. Goubanova et al. (2018) and Patricola et al. (2012), for example, point to an equatorial westerly wind bias as the major contributor to incorrect thermocline depth representation and its influence on SST in the eastern tropical Atlantic. Harlaß et al. (2018) showed that models with high horizontal and vertical atmospheric resolution had improved wind structure that correctly simulated the development of the equatorial cold tongue during the boreal spring and summer by allowing more realistic thermocline depth variation and latitudinal position of the ITCZ. However, higher atmospheric resolution alone does not completely eliminate SST biases in coupled climate model simulations of the tropical Atlantic (Doi et al., 2012), suggesting that improved cloud parametrizations are important for improving the simulation of cloud radiative feedbacks and their effects on SST. To quantify the significance of various factors in coupled climate models that lead to systematic warm biases in the eastern tropical Atlantic, model-based mixed layer heat budget analyses complimentary to that presented in this paper need to be undertaken in a future study.

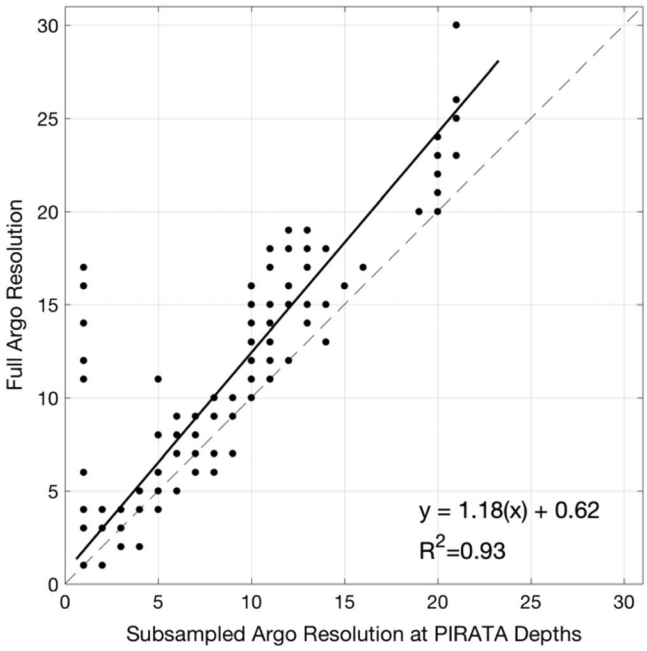

Figure A2. Linear regression of mixed layer depth between Argo profiles at full vertical resolution and Argo profiles subsampled at Prediction and Research Moored Array in the Atlantic depths.

Appendix A: Mixed Layer Depth Correction Using Argo Floats

The calculation of mixed layer depth (MLD) is adjusted using 186 temperature and salinity profiles from neighboring Argo floats with ±2° latitude and longitude of 6°S, 8°E. Compared to the relatively coarse vertical resolution of PIRATA near the surface (1, 5, 10, 20, 40 m for temperature and salinity), Argo has a vertical sampling scheme of ~2 dbar in the upper 50 m. Buoy temperature and salinity data from 3 m were not used for this correction because of the short record of observations at 3 m for comparison with the Argo profiles. Argo accuracy is ±0.005 °C, ±0.01 salinity units, and 2.5 dbar for subsurface temperature, salinity, and pressure, respectively (Riser et al., 2016).

We compare MLDs using a density-defined criteria of a 0.08 kg/m^3 density equivalent increase from a 1-m reference level (section 2.2) using subsampled Argo data at the PIRATA sampling depths and the full-resolution Argo data (Figure A1). We use a least squares fit linear regression to quantify the error in MLD computed using the more coarsely resolved PIRATA data (Figure A2). Subsampled Argo data on average yield mixed layers

that are 18% too shallow with a constant offset of 0.62 m. We correct the PIRATA mixed layer depths at 6°S, 8°E using a regression equation based on the Argo data. Once applied to the PIRATA data, this becomes an adjusted mixed layer depth used throughout the remainder of the analysis (Figure A1). The root-mean-square errors in the adjusted PIRATA MLDs compared to the MLDs computed using the full Argo resolution are 1.25 m in the upper 5 m, 1.25 m between 5 and 10 m, 2.07 m between 10 and 20 m, and 2.92 m between 20 and 30 m.

Acknowledgments
We acknowledge the Institut de Recherche Scientifique pour le Développement en Coopération (IRD) and Meteo-France in France, the Instituto Nacional de Pesquisas Espaciais (INPE) and Diretoria de Hidrografia e Navegacao (DHN) in Brazil and NOAA in the United States for support of PIRATA. Partial financial support for the 6°S, 8°E mooring was provided by the EU PREFACE (Enhancing PREdiction oF tropical Atlantic ClimatE and its impacts) program. This study was supported by NOAA's office of Oceanic and Atmospheric Research. PIRATA data were downloaded from the NOAA Global Tropical Moored Buoy Array at https://www.pmel.noaa.gov/gtmba/pirata. Data from the NASA MODIS Aqua and Terra missions can be found from https://modis.gsfc.nasa.gov/. NOAA high-resolution SST and CMAP precipitation data were provided by the NOAA/OAR/ESRL PSD from their website at http://www.esrl.noaa.gov/psd/. Data from TropFlux are from the Indian National Centre for Ocean Information Services and their website http://www.incois.gov.in/tropflux/. This is a PMEL contribution 4757.

References

A'Hearn, P. N., Freitag, H. P., & McPhaden, M. J. (2002). ATLAS module temperature bias due to solar heating (NOAA Technical Memorandum OAR PMEL-121). Seattle, WA: NOAA Pacific Marine Environmental Laboratory.

Bachèlery, M. -L., Illig, S., & Dadou, I. (2016). Interannual variability in the South-East Atlantic Ocean, focusing on the Benguela Upwelling System: Remote versus local forcing. *Journal of Geophysical Research: Oceans*, *121*, 284–310. https://doi.org/10.1002/2015JC011168

Badescu, V. (1997). Verification of some very simple clear and cloudy sky models to evaluate global solar irradiance. *Solar Energy*, *61*(4), 251–264. https://doi.org/10.1016/S0038-092X(97)00057-1

Bourles, B., Lumpkin, R., McPhaden, M. J., Hernandez, F., Nobre, R., Campos, E., et al. (2008). The PIRATA program history, accomplishments, and future direction. *Bulletin of the American Meteorological Society*, *89*(8), 1111–1126. https://doi.org/10.1175/2008BAMS2462.1

Camara, I., Kolodziejczyk, N., Mignot, J., Lazar, A., & Gaye, A. T. (2015). On the seasonal variations of salinity of the tropical Atlantic mixed layer. *Journal of Geophysical Research: Oceans*, *120*, 4441–4462. https://doi.org/10.1002/2015JC010865

Carton, J. A., & Zhou, Z. X. (1997). Annual cycle of sea surface temperature in the tropical Atlantic Ocean. *Journal of Geophysical Research*, *102*(C13), 27,813–27,824. https://doi.org/10.1029/97JC02197

Chang, P. (1993). Seasonal cycle of sea surface temperature and mixed layer heat budget in the tropical Pacific Ocean. *Geophysical Research Letters*, *20*(19), 2079–2082. https://doi.org/10.1029/93GL02374

Cronin, M. F., & McPhaden, M. J. (1997). The upper ocean heat balance in the western equatorial Pacific warm pool during September-December 1992. *Journal of Geophysical Research*, *102*(C4), 8533–8553. https://doi.org/10.1029/97JC00020

Da-Allada, C. Y., Alory, G., du Penhoat, Y., Kestenare, E., Durand, F., & Hounkonnou, N. M. (2013). Seasonal mixed-layer salinity balance in the tropical Atlantic Ocean: Mean state and seasonal cycle. *Journal of Geophysical Research: Oceans*, *118*, 332–345. https://doi.org/10.1029/2012JC008357

De Coëtlogon, G., Leduc-Leballeur, M., Meynadier, R., Bastin, S., Diakhaté, M., Eymard, L., et al. (2013). Atmospheric response to sea-surface temperature in the eastern equatorial Atlantic at quasi-biweekly time-scales. *Quarterly Journal of the Royal Meteorological Society*, *140*, 1700–1714. https://doi.org/10.1002/qj.2250

Ding, H., Keenlyside, N. S., & Latif, M. (2009). Seasonal cycle in the upper equatorial Atlantic Ocean. *Journal of Geophysical Research*, *114*, C09016. https://doi.org/10.1029/2009JC005418

Doi, T., Vecchi, G. A., Rosati, A. J., & Delworth, T. L. (2012). Biases in the Atlantic ITCZ in seasonal-interannual variations for a coarse- and a high-resolution coupled climate model. *Journal of Climate*, *25*(16), 5494–5511. https://doi.org/10.1175/JCLI-D-11-00360.1

Edson, J. B., Jampana, V., Weller, R. A., Bigorre, S. P., Plueddemann, A. J., Fairall, C. W., et al. (2013). On the exchange of momentum over the open ocean. *Journal of Physical Oceanography*, *43*(8), 1589–1610. https://doi.org/10.1175/JPO-D-12-0173.1

Exarchou, E., Prodhomme, C., Brodeau, L., Guemas, V., & Doblas-Reyes, F. (2017). Origin of the warm eastern tropical Atlantic SST bias in a climate model. *Climate Dynamics*. https://doi.org/10.1007/s00382-017-3984-3

Fairall, C. W., Bradley, E. F., Hare, J. E., Grachev, A. A., & Edson, J. B. (2003). Bulk parameterization of air-sea fluxes: Updates and verification for the COARE algorithm. *Journal of Climate*, *16*(4), 571–591. https://doi.org/10.1175/1520-0442(2003)016%3C0571:BPOASF%3E2.0.CO;2

Florenchie, P., Lutjeharms, J. R. E., Reason, C. J. C., Masson, S., & Rouault, M. (2003). The source of Benguela Niños in the South Atlantic Ocean. *Geophysical Research Letters*, *30*(10), 1505. https://doi.org/10.1029/2003GL017172

Foltz, G. R., Grodsky, S. A., & Carton, J. A. (2003). Seasonal mixed layer heat budget of the tropical Atlantic Ocean. *Journal of Geophysical Research*, *108*(C5), 3146. https://doi.org/10.1029/2002JC001584

Foltz, G. R., & McPhaden, M. J. (2009). Impact of barrier layer thickness on SST in the central tropical North Atlantic. *Journal of Climate*, *22*(2), 285–299. https://doi.org/10.1175/2008JCLI2308.1

Foltz, G. R., Schmid, C., & Lumpkin, R. (2013). Seasonal cycle of the mixed layer heat budget in the northeastern tropical Atlantic Ocean. *Journal of Climate*, *26*(20), 8169–8188. https://doi.org/10.1175/JCLI-D-13-00037.1

Freitag, H. P., Feng, Y., Mangum, L. J., McPhaden, M. P., Neander, J., & Stratton, L. D. (1995). Calibration procedures and instrumental accuracy estimates of TAO temperature, relative humidity and radiation measurements (NOAA Technical Memorandum ERL PMEL-104). Seattle, WA: NOAA Pacific Marine Environmental Laboratory.

Freitag, H. P., McCarty, M. E., Nosse, C., Lukas, R., McPhaden, M. J., & Cronin, M. F. (1999). COARE Seacat data: Calibrations and quality control procedures (NOAA Technical Memorandum ERL PMEL-115). Seattle, WA: NOAA Pacific Marine Environmental Laboratory.

Freitag, H. P., Ning, C., Berk, P., Dougherty, D., Marshall, R., Strick, J. M., & Zimmerman, D. (2016). ATLAS, T-Flex, BaiLong meteorological sensor comparison test report (NOAA Technical Memorandum OAR PMEL-148). Seattle, WA: NOAA Pacific Marine Environmental Laboratory.

Freitag, H. P., O'Haleck, M., Thomas, G. C., & McPhaden, M. J. (2001). Calibration procedures and instrumental accuracies for ATLAS wind measurements (NOAA Technical Memorandum OAR PMEL-119). Seattle, WA: NOAA Pacific Marine Environmental Laboratory.

Goubanova, K., Sanchez-Gomez, E., Frauen, C., & Voldoire, A. (2018). Respective roles of remote and local wind stress forcings in the development of warm SST errors in the south-eastern tropical Atlantic in a coupled high-resolution model. *Climate Dynamics*. https://doi.org/10.1007/s00382-018-4197-0

Harlaß, J., Latif, M., & Park, W. (2018). Alleviating tropical Atlantic sector biases in the Kiel climate model by enhancing horizontal and vertical atmosphere model resolution: Climatology and interannual variability. *Climate Dynamics*, *50*(7-8), 2605–2635. https://doi.org/10.1007/s00382-017-3760-4

Hayes, S. P., McPhaden, M. J., & Wallace, J. M. (1989). The influence of sea-surface temperature on surface wind in the eastern equatorial Pacific: Weekly to monthly variability. *Journal of Climate*, *2*(12), 1500–1506. https://doi.org/10.1175/1520-0442(1989)002%3C1500:TIOSST%3E2.0.CO;2

Kumar, B. P., Vialard, J., Lengaigne, M., Murty, V. S. N., McPhaden, M. J., Cronin, M. F., et al. (2013). TropFlux wind stresses over the tropical oceans: Evaluation and comparison with other products. *Climate Dynamics*, *40*(7-8), 2049–2071. https://doi.org/10.1007/s00382-012-1455-4

Lake, B. J., Noor, S. M., Freitag, H. P., & McPhaden, M. J. (2003). Calibration procedures and instrumental accuracy estimates of ATLAS air temperature and relative humidity measurements (NOAA Technical Memorandum OAR PMEL-123). Seattle, WA: NOAA Pacific Marine Environmental Laboratory.

Li, T., & Philander, S. G. H. (1997). On the seasonal cycle of the equatorial Atlantic Ocean. *Journal of Climate*, *10*(4), 813–817. https://doi.org/10.1175/1520-0442(1997)010%3C0813:OTSCOT%3E2.0.CO;2

Lübbecke, J. F., Böning, C. W., Keenlyside, N. S., & Xie, S.-P. (2010). On the connection between Benguela and equatorial Atlantic Niños and the role of the South Atlantic anticyclone. *Journal of Geophysical Research*, *115*, C09015. https://doi.org/10.1029/2009JC005964

McPhaden, M. J. (1982). Variability in the central equatorial Indian Ocean. Part II: Oceanic heat and turbulent energy balance. *Journal of Marine Research*, *40*, 403–419.

Mitchell, T. P., & Wallace, J. M. (1992). On the annual cycle in equatorial convection and sea surface temperature. *Journal of Climate*, *5*(10), 1140–1156. https://doi.org/10.1175/1520-0442(1992)005%3C1140:TACIEC%3E2.0.CO;2

Moisan, J. R., & Niiler, P. P. (1998). The seasonal heat budget of the North Pacific: Net heat flux and heat storage rates (1950-1990). *Journal of Physical Oceanography*, *28*(3), 401–421. https://doi.org/10.1175/1520-0485(1998)028%3C0401:TSHBOT%3E2.0.CO;2

Morel, A. (1988). Optical modeling of the upper ocean in relation to its biogenous matter content (case I waters). *Journal of Geophysical Research*, *93*(C9), 10,749–10,768. https://doi.org/10.1029/JC093iC09p10749

Patricola, C. M., Li, M., Xu, Z., Change, P., Saravanan, R., & Hsieh, J.-S. (2012). An investigation of tropical Atlantic bias in a high-resolution coupled regional climate model. *Climate Dynamics*, *39*(9-10), 2443–2463. https://doi.org/10.1007/s00382-012-1320-5

Plimpton, P. E., Freitag, H. P., & McPhaden, M. J. (1995). Correcting moored ADCP data for fish-bias errors at 0,110W and 0,140W from 1990 to 1993 (NOAA Technical Memorandum ERL PMEL-107). Seattle, WA: NOAA Pacific Marine Environmental Laboratory.

Plimpton, P. E., Freitag, H. P., & McPhaden, M. J. (2004). Processing of subsurface ADCP data in the equatorial Pacific (NOAA Technical Memorandum OAR PMEL-125). Seattle, WA: NOAA Pacific Marine Environmental Laboratory.

Qu, X., Hall, A., Klein, S. A., & Caldwell, P. M. (2014). On the spread of changes in marine low cloud cover in climate model simulations of the 21st century. *Climate Dynamics*, *42*(9-10), 2603–2626. https://doi.org/10.1007/s00382-013-1945-z

Reynolds, R. W., Smith, T. M., Liu, C., Chelton, D. B., Casey, K. S., & Schlax, M. G. (2007). Daily high-resolution-blended analyses for sea surface temperature. *Journal of Climate*, *20*(22), 5473–5496. https://doi.org/10.1175/2007JCLI1824.1

Richter, I. (2015). Climate model biases in the eastern tropical oceans: Causes, impacts and ways forward. *WIREs Climate Change*, *6*(3), 345–358. https://doi.org/10.1002/wcc.338

Richter, I., Behera, S. K., Masumoto, Y., Taguchi, B., Komori, N., & Yamagata, T. (2010). On the triggering of Benguela Niños: Remote equatorial versus local influences. *Geophysical Research Letters*, *37*, L20604. https://doi.org/10.1029/2010GL044461

Riser, S. C., Freeland, H. J., Roemmich, D., Wijffels, S., Troisi, A., Belbéoch, M., et al. (2016). Fifteen years of ocean observations with the global Argo array. *Nature Climate Change*, *6*, 145–153. https://doi.org/10.1038/nclimate2872

Rouault, M., Illig, S., Bartholomae, C., Reason, C. J. C., & Bentamy, A. (2007). Propagation and origin of warm anomalies in the Angola Benguela upwelling system in 2001. *Journal of Marine Systems*, *68*(3–4), 473–488. https://doi.org/10.1016/j.jmarsys.2006.11.010

Rouault, M., Servain, J., Reason, C. J. C., Bourles, B., Rouault, M. J., & Fauchereau, N. (2009). Extension of PIRATA in the tropical south-east Atlantic: An initial one-year experiment. *African Journal of Marine Science*, *31*(1), 63–71. https://doi.org/10.2989/AJMS.2009.31.1.5.776

Serra, Y. L., A'Hearn, P., Freitag, H. P., & McPhaden, M. J. (2001). ATLAS self-siphoning rain gauge error estimates. *Journal of Atmospheric and Oceanic Technology*, *18*(12), 1989–2002. https://doi.org/10.1175/1520-0426(2001)018%3C1989:ASSRGE%3E2.0.CO;2

Servain, J., Busalacchi, A. J., McPhaden, M. J., Moura, A. D., Reverdin, G., Vianna, M., & Zebiak, S. E. (1998). A Pilot Research Moored Array in the Tropical Atlantic (PIRATA). *Bulletin of the American Meteorological Society*, *79*(10), 2019–2031. https://doi.org/10.1175/1520-0477(1998)079%3C2019:APRMAI%3E2.0.CO;2

Sherwood, S. C., Bony, S., & Dufresne, J.-L. (2014). Spread in model climate sensitivity traced to atmospheric convective mixing. *Nature*, *505*(7481), 37–42. https://doi.org/10.1038/nature12829

Smith, S. D. (1988). Coefficients for sea surface wind stress, heat flux, and wind profiles as a function of wind speed and temperature. *Journal of Geophysical Research*, *93*(C12), 15,467–15,472. https://doi.org/10.1029/JC093iC12p15467

Sprintall, J., & Tomczak, M. (1992). Evidence of the barrier layer in the surface layer of the tropics. *Journal of Geophysical Research*, *97*(C5), 7305–7316. https://doi.org/10.1029/92JC00407

Stevenson, J. W., & Niiler, P. P. (1983). Upper Ocean heat budget during the Hawaii-to-Tahiti shuttle experiment. *Journal of Physical Oceanography*, *13*(10), 1894–1907. https://doi.org/10.1175/1520-0485(1983)013%3C1894:UOHBDT%3E2.0.CO;2

Tzortzi, E., Josey, S. A., Srokosz, M., & Gommenginger, C. (2013). Tropical Atlantic salinity variability: New insights from SMOS. *Geophysical Research Letters*, *40*, 2143–2147. https://doi.org/10.1002/grl.50225

Wallace, J. M., Mitchell, T. P., & Deser, C. (1989). The influence of sea surface temperature on surface wind in the eastern equatorial Pacific: Seasonal and interannual variability. *Journal of Climate*, *2*(12), 1492–1499. https://doi.org/10.1175/1520-0442(1989)002%3C1492:TIOSST%3E2.0.CO;2

Wang, W., & McPhaden, M. J. (1999). The surface-layer heat balance in the equatorial Pacific Ocean. Part I: Mean seasonal cycle. *Journal of Physical Oceanography*, *29*, 1812–1831. https://doi.org/10.1175/1520-0485(1999)029%3C1812:TSLHBI%3E2.0.CO;2

Weisberg, R. H., & Tang, T. Y. (1990). A linear analysis of equatorial Atlantic Ocean thermocline variability. *Journal of Physical Oceanography*, *20*(12), 1813–1825. https://doi.org/10.1175/1520-0485(1990)020%3C1813:ALAOEA%3E2.0.CO;2

Wood, R. (2012). Review: Stratocumulus clouds. *Monthly Weather Review*, *140*(8), 2373–2423. https://doi.org/10.1175/MWR-D-11-00121.1

Xie, S.-P., & Carton, J. A. (2004). Tropical Atlantic variability: Patterns, mechanisms, and impacts. In C. Wang, S.-P. Xie, & J. A. Carton (Eds.), *Earth's climate: The ocean-atmosphere interaction*, *Geophysical Monography* (Vol. 147, pp. 121–142). Washington, D.C.: AGU Press. https://doi.org/10.1029/147GM07

Yamagata, T., & Iizuka, S. (1995). Simulation of the tropical thermal domes in the Atlantic: A seasonal cycle. *Journal of Physical Oceanography*, *25*(9), 2129–2140. https://doi.org/10.1175/1520-0485(1995)025%3C2129:SOTTTD%3E2.0.CO;2

Yu, L., Jin, X., & Weller, R. A. (2006). Role of net surface heat flux in seasonal variations of sea surface temperature in the tropical Atlantic Ocean. *Journal of Climate*, *19*(23), 6153–6169. https://doi.org/10.1175/JCLI3970.1

Zuidema, P., Chang, P., Medeiros, B., Kirtman, B. P., Mechoso, R., Schneider, E. K., et al. (2016). Challenged and prospects for reducing coupled climate model SST biases in the eastern tropical Atlantic and Pacific Oceans. *Bulletin of the American Meteorological Society*, *97*(12), 2305–2328. https://doi.org/10.1175/BAMS-D-15-00274.1